

See discussions, stats, and author profiles for this publication at: <https://www.researchgate.net/publication/231241143>

Synthesis of Ligand-Stabilized Silicon Nanocrystals with Size-Dependent Photoluminescence Spanning Visible to Near-Infrared Wavelengths

ARTICLE in CHEMISTRY OF MATERIALS · DECEMBER 2011

Impact Factor: 8.35 · DOI: 10.1021/cm2032866

CITATIONS

92

READS

48

9 AUTHORS, INCLUDING:



Matthew Panthani

University of Chicago

34 PUBLICATIONS 1,770 CITATIONS

SEE PROFILE



Michael R Rasch

University of Texas at Austin

17 PUBLICATIONS 592 CITATIONS

SEE PROFILE



Junwei Wei

University of Texas at Austin

12 PUBLICATIONS 152 CITATIONS

SEE PROFILE

Synthesis of Ligand-Stabilized Silicon Nanocrystals with Size-Dependent Photoluminescence Spanning Visible to Near-Infrared Wavelengths

Colin M. Hessel,[†] Dariya Reid,[†] Matthew G. Panthani,[†] Michael R. Rasch,[†] Brian W. Goodfellow,[†] Junwei Wei,[‡] Hiromasa Fujii,[§] Vahid Akhavan,[†] and Brian A. Korgel^{*,†}

[†]Department of Chemical Engineering, Texas Materials Institute, and Center for Nano- and Molecular Science and Technology and

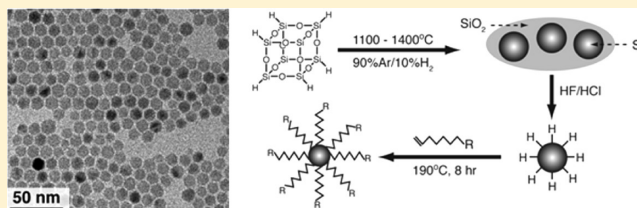
[‡]Department of Physics, The University of Texas at Austin, Austin, Texas 78712, United States

[§]Department of Electrical Engineering and Information Systems, School of Engineering, The University of Tokyo, Tokyo, Japan

Supporting Information

ABSTRACT: We report a chemical route to colloidal silicon (Si) nanocrystals, or quantum dots, with widely tunable average diameter, from less than 3 nm up to 90 nm and peak photoluminescence (PL) from visible wavelengths to the bulk band gap of Si at 1100 nm. The synthesis relies on the high temperature (>1100 °C) decomposition of hydrogen silsesquioxane (HSQ) to obtain Si quantum dots with good crystallinity and a narrow size distribution with tunable size embedded in SiO₂. The oxide matrix is removed by hydrofluoric acid etching in the dark. Subsequent thermal hydrosilylation with alkenes yields free, solvent-dispersible Si nanocrystals with bright PL. The relationship between PL energy and size, exhaustively characterized by transmission electron microscopy (TEM), small-angle X-ray scattering (SAXS), and X-ray diffraction (XRD), is reported.

KEYWORDS: silicon nanocrystals, hydrogen silsesquioxane, HSQ, size determination, small-angle X-ray scattering, SAXS, Scherrer analysis, X-ray diffraction, XRD, transmission electron microscopy, TEM



INTRODUCTION

Silicon (Si) is the foundation of the semiconductor industry, with use in devices ranging from transistors and memory elements to photodetectors and photovoltaics. But Si is a poor light emitter because of its indirect band gap, making it unsuitable for applications requiring luminescence, like light-emitting diodes (LEDs) and lasers. Even so, light emission can be coaxed from Si by reducing its dimensions to the nanoscale. Quantum confinement eliminates the conservation of crystal momentum and the optical transitions of a Si nanostructure become spectroscopically allowed, with photophysical properties more like those of direct gap semiconductors.^{1,2} After Canham¹ observed room-temperature photoluminescence (PL) from porous Si in 1990, light emission from Si nanostructures has been studied extensively. Size-dependent PL has been reported with color spanning much of the visible spectrum,^{3–6} and Si nanocrystals have been implemented in LEDs^{7–9} and as biocompatible and biodegradable fluorescent optical contrast agents for biological imaging and in vivo disease detection.^{10–13}

Nonetheless, significant fundamental questions remain regarding light emission from Si nanocrystals. For example, the upper size threshold for efficient light emission from Si is not accurately known, data in the literature correlating the size and color of PL from Si nanocrystals varies widely, and the influence of surface chemistry on the PL of Si nanocrystals remains highly unpredictable. Most of these problems persist

because luminescent *colloidal* Si nanocrystals remain difficult to make, despite the significant advances in nanomaterials chemistry that have been made during the past 25 years for other semiconductors. A number of chemical approaches to colloidal ligand-stabilized Si nanocrystals currently exist,^{14–18} and still new methods continue to appear,^{3,18–30} but these methods generally lack the ability to widely vary size and PL. In cases where size could be varied and size-dependent PL was observed, only a very narrow range of nanocrystal sizes (and PL energies) could be obtained from the synthesis.^{3,18,25,29,30} In a number of other reports, the PL of colloidal produced Si nanocrystals has not been size-dependent at all, with nanocrystals emitting only blue light at wavelengths less than 480 nm.^{19–24} The surface chemistry of Si nanocrystals can also have a significant effect on the color of the PL and has been another source of confusion and significant disagreement in the literature. For instance, differences in surface passivation and the presence of oxygen can shift the PL emission of similar-sized nanocrystals by more than 100 nm in wavelength.^{31,32} A synthetic route with the ability to generate a wide size range of light-emitting Si nanocrystals with similar surface chemistry would be very useful. Here, we report such a synthetic method:

Received: November 2, 2011

Revised: December 1, 2011

Published: December 7, 2011



one that generates Si nanocrystals with diameter that can be systematically tuned from just under 3 nm up to 90 nm with similar organic ligand surface stabilization chemistry.

Another problem is that the size of Si nanocrystals is not straightforward to obtain. Most often, sizing of Si nanocrystals is done by transmission electron microscopy (TEM). Yet it is challenging to get accurate size information by TEM because of the low imaging contrast due to the relatively small difference in atomic number between Si and the underlying carbon support layer (i.e., *z*-contrast). Furthermore, the typical capping ligands for Si nanocrystals, like octadecene and other long-chain alkenes, have extremely low volatility, making it difficult to purify the nanocrystals from free capping ligand that further obscures the images. Here, we show that graphene as a TEM support can provide clear images of Si nanocrystals. We also show that, with relatively monodisperse samples, additional complementary characterization techniques of small-angle X-ray scattering (SAXS) and X-ray diffraction (XRD) provide an accurate determination of nanocrystal size.

The Si nanocrystal synthesis reported here extends an approach developed at the University of Alberta in 2006.³ Hydrogen silsesquioxane (HSQ)—a silicon suboxide—is heated to form Si nanocrystals embedded in an oxide matrix. The nanocrystal size can be varied over a wide range by changing the temperature used to decompose the HSQ. The largest nanocrystals, of nearly 90 nm in diameter, are obtained by heating at 1400 °C, just below the melting point of Si. The nanocrystals are then liberated from the oxide by etching with HF. Etching in the dark enables the oxide to be removed with high selectivity and no decrease in nanocrystal size. The resulting H-terminated nanocrystals are then passivated with alkenes by thermal hydrosilylation. The nanocrystals have narrow size distributions and luminesce with relatively high quantum yield (1–10%), even in the larger size ranges when the emission is close to the bulk band gap energy. The PL color could be tuned by this same synthetic procedure from 700 nm to nearly 1100 nm. The nanocrystal size was determined with TEM imaging on graphene supports and complementary SAXS and XRD analysis to provide an accurate correlation between PL energy and nanocrystal size.

■ EXPERIMENTAL DETAILS

Materials. FOx 16 (Dow Corning Corporation, 16% HSQ by weight in methyl isobutyl ketone), ethanol (Sigma, 99%), methanol (Sigma, 99%), hydrofluoric acid (Sigma, 48%), 1-dodecene (Acros Organics, 93%), 1-octadecene (Aldrich, 90%), toluene (Fisher, 99.9%), acetone (Fisher, 99.9%), hydrochloric acid (Fischer, 25%), IR-26 (Exciton Corp., 100%), and 0.1 mg of graphene in 1 mL of ethanol (Electron Microscopy Sciences) were purchased and used as received.

Oxide-Embedded Si Nanocrystals. Si nanocrystals are first obtained by thermal decomposition of HSQ.^{3,13,33} Solid white HSQ (5.0 g) is placed in a quartz crucible and heated at a rate of 18 °C/min under a flow of 90% Ar/10% H₂ to a peak processing temperature between 1100 and 1400 °C, depending on the desired nanocrystal size. The sample is held at the peak processing temperature for 1 h before the furnace is allowed to cool to room temperature. A brown/black glassy product is obtained. This product is ground for 20 min in an agate mortar and pestle to obtain a brown powder with a grain size of about 2 μm. The grain size is then further reduced to ~200 nm by shaking in a wrist-action shaker for 9 h with 30 g of 3 mm borosilicate glass beads. Mechanical reduction of the oxide-

embedded Si nanocrystal grain size is essential for uniform etching of the oxide matrix.

Oxide Etching to Liberate Si Nanocrystals. Ground powder of oxide-embedded Si nanocrystals (300 mg) is suspended in a solution of 13 mL of 48% HF and 2 mL of 25% HCl in the dark for 6 h. This procedure etches the oxide and yields hydride-terminated Si nanocrystals. The nanocrystals are isolated from the HF solution by centrifugation at 9000 rpm for 3 min.

Si Nanocrystal Alkene Surface Passivation. After centrifugation, the supernatant is discarded and the light-brown precipitate is rinsed twice with 5 mL of ethanol and once with 5 mL of toluene and finally dispersed in 8 mL of 1-dodecene and 2 mL of 1-octadecene. The resulting brown, turbid dispersion is transferred to a three-neck round-bottom flask and degassed with 4 freeze–pump–thaw cycles on a greaseless Schlenk line. The dispersion is heated at 190 °C for 8 h. After about 30 min of heating, the turbid brown dispersion turns to an optically clear dark-orange dispersion. The alkene-passivated Si nanocrystals are washed three times by precipitation with acetone as an antisolvent (15 mL) and dispersed in 1 mL of toluene. The concentrated nanocrystal dispersions are then heated under vacuum for 24 h at 200 °C to remove excess ligand. The nanocrystals are finally dispersed in toluene for subsequent characterization. The mass yield of ligand stabilized Si nanocrystals is about 10% with respect to the oxide-embedded Si nanocrystal powder.

Material Characterization. Low-resolution transmission electron microscopy (TEM) images were acquired digitally on a FEI Tecnai Spirit Bio Twin operated at 80 kV. TEM samples were prepared by drop-coating a 5 μL aliquot of a very dilute Si nanocrystal dispersion onto carbon-coated copper 200 mesh TEM grids (Electron Microscopy Sciences). Bright-field and high-angle annular dark-field scanning tunneling electron microscopy (STEM) images were acquired digitally on a JEOL model JEM-ARM200F instrument operated at 120 kV. STEM samples were prepared by drop-coating a 3 μL aliquot of 0.1 mg of graphene in 1 mL of ethanol onto a lacey carbon grid (lacey carbon-coated copper, Electron Microscopy Sciences), and allowed to dry for 1 h. A 5 μL aliquot of a very dilute Si nanocrystal dispersion was then drop-coated onto the graphene-coated grid and heated at 200 °C for 8 h under a dynamic flow of N₂.

X-ray photoelectron spectroscopy (XPS) was performed on a Kratos photoelectron spectrometer equipped with a charge neutralizer and 180° hemispherical electron energy analyzer. XPS samples were prepared by drop-casting Si nanocrystals (~5 mg) onto indium tin oxide (ITO) coated glass substrates and degassing at 10^{−7} Torr for 1 day prior to analysis. XPS data were internally standardized with respect to the O 1s peak position (530 eV).

X-ray diffraction (XRD) was performed on a Rigaku R-Axis Spider diffractometer with an image plate detector using Cu Kα radiation ($\lambda = 1.5418$ Å) and a graphite monochromator. The instrument was controlled by Rapid/XRD diffractometer control software (version 2.3.8, Rigaku Americas Corp., The Woodlands, TX). 2DP Spider software (version 1.0, Rigaku Americas Corp., The Woodlands, TX) was used to integrate the two-dimensional image into a one-dimensional pattern. XRD samples were prepared by mixing a small amount (≤ 1 mg) of dried Si nanocrystals with a drop of mineral oil and mounting the mixture on a Hampton Research cryoloop. XRD patterns were collected for ~15 min.

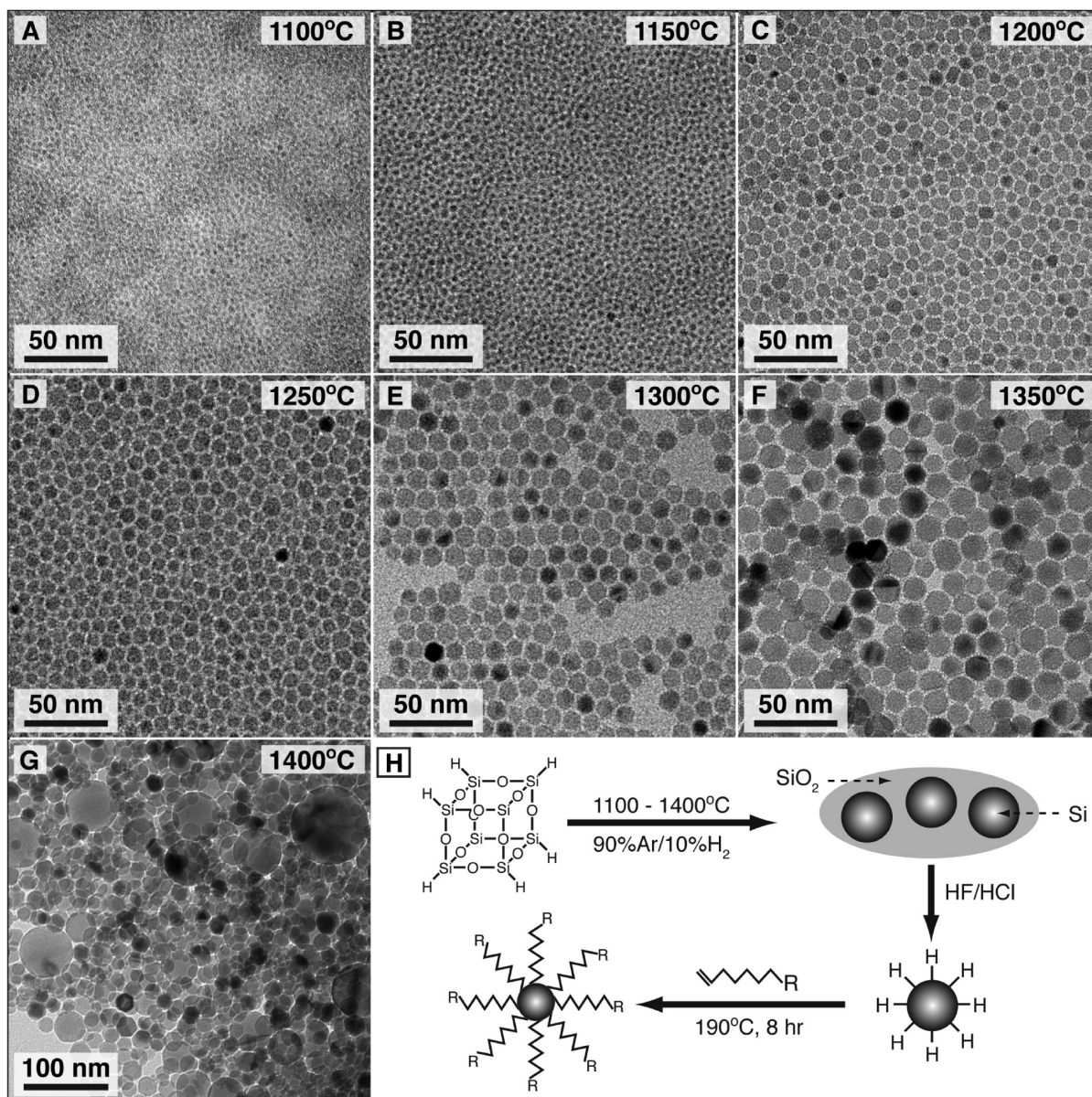


Figure 1. (A–G) TEM images of alkene-passivated Si nanocrystals generated by HSQ decomposition at the indicated temperatures. (H) Synthetic pathway from HSQ to alkyl passivated Si nanocrystals.

Small-angle X-ray scattering (SAXS) measurements were performed on a Molecular Metrology system with a rotating copper anode X-ray generator (Bruker Nonius; $\lambda = 1.54 \text{ \AA}$) operating at 3.0 kW. SAXS samples were prepared by loading Si nanocrystals dispersed in toluene into a stainless steel cell enclosed with Kapton windows. The scattered X-rays were collected on a 2D multiwire gas-filled detector (Molecular Metrology, Inc.), and the scattering angle was calibrated by use of a silver behenate $[\text{CH}_3(\text{CH}_2)_{20}\text{COOAg}]$ standard. Radial integrations of scattering intensity were performed with Datasqueeze. Experimental data were corrected for background scattering through toluene.

Optical absorbance spectroscopy was performed at room temperature on a Cary 500 ultraviolet–visible–near-infrared (UV–vis–NIR) spectrophotometer in a quartz cuvette with a 10 mm optical path length. Photoluminescence (PL) and photoluminescence excitation (PLE) spectra were acquired on a Fluorolog-3 spectrophotometer (Horiba Jobin Yvon) by use

of a monochromated 450 W xenon lamp light source with an InGaAs photomultiplier tube for visible detection and a Hamamatsu H10330-45 detector for NIR detection. Both detectors were thermoelectrically cooled. A reference silicon photodiode was used to adjust for intensity differences in the lamp spectrum for PLE measurements. The PL quantum yield (QY) was determined by comparing the integrated photon count of nanocrystal samples to IR-26, a NIR-emitting dye with a quantum yield of 0.05%, similar to ref 30.³⁴ Although this dye is not ideal because it has a relatively low quantum yield of only 0.05%, there are very few NIR-emitting dyes available. The details of the QY calculations are included in the Supporting Information. PL spectra of IR-26 were obtained from chloroform solutions with an excitation wavelength of 980 nm. PL spectra of Si nanocrystals were obtained from toluene dispersions photoexcited at 400 nm. The Si nanocrystal concentration was adjusted to ensure that the absorbance for all measurements was less than 0.1 between 700 and 1100 nm.

Thermogravimetric analysis (TGA) was performed on a Mettler Toledo model TGA/DSC 1 with alumina crucibles (Mettler Toledo). The 70 μL crucibles were cleaned by sonication for 15 min in concentrated nitric acid and rinsed with deionized water before being baked at 800 $^{\circ}\text{C}$ in air for 45 min. A 70 μL aliquot of Si nanocrystals dispersed in chloroform at 15 mg/mL was added to the crucible and the solvent was allowed to evaporate, providing roughly 1 mg of dry Si nanocrystals in the crucible. The sample was heated from 25 to 800 at 3 $^{\circ}\text{C}/\text{min}$ under nitrogen gas flowing at 5 mL/min. TGA/DSC simultaneously recorded the heat flow and crucible mass versus time and temperature.

RESULTS AND DISCUSSION

Oxide-Embedded Growth of Si Nanocrystals. Figure 1H illustrates the synthetic steps employed to obtain ligand-stabilized colloidal Si nanocrystals: (1) high-temperature decomposition of HSQ into oxide-embedded Si nanocrystals; (2) oxide etching in the dark by HF to liberate H-terminated Si nanocrystals; and (3) thermal hydrosilylation with a long-chain alkene. The nanocrystal size is governed by the HSQ decomposition temperature. Higher temperatures (above 1100 $^{\circ}\text{C}$) lead to larger nanocrystals. Hessel et al.^{3,29} reported similar HSQ decomposition to obtain Si nanocrystals, but they obtained different nanocrystal sizes by use of a two-step heating procedure in which nanocrystals were first nucleated at 1100 $^{\circ}\text{C}$ and then ripened to larger size at 1200 and 1400 $^{\circ}\text{C}$. The use of a single heating step is important. First of all, the single-step synthesis reduces the reaction time by a factor of 2 compared to the two-step heating method. Uninterrupted heating in the single-step method also yields nanocrystals with a much narrower size distribution than two-step heating and access to larger nanocrystals at identical reaction temperatures. Combined nucleation and growth at higher temperature in the single-step heating method appears to lead to an important and influential change in nanocrystal growth mechanism.

Si Nanocrystal Liberation from the Silica Matrix by Etching. The SiO_2 matrix was dissolved to yield freestanding, hydride-terminated Si nanocrystals by etching the as-made oxide-embedded nanocrystals in the dark with a solution containing hydrofluoric and hydrochloric acids. Unlike previous etching recipes related to Si nanocrystals that have been designed to decrease the nanocrystal size by use of intense light or chemical additives such as ethanol or nitric acid,^{35,36} this procedure was designed to specifically remove SiO_2 while preserving the nanocrystal size and morphology. HF can react with both SiO_2 and Si. The etching selectivity for SiO_2 compared to Si is enhanced by performing the etching in the dark, as the Si etch rate is significantly decreased in the absence of light to create photoexcited holes in the valence band.³⁷ The presence of photoexcited holes in the Si valence band is required to initiate nonelectrochemical etching of Si.^{38,39} After etching, the hydrogen-terminated Si nanocrystals form large aggregates in solution and will oxidize in ambient atmosphere. To enhance colloidal stability and prevent surface oxidation, the surface-hydrogenated Si nanocrystals were chemically modified with chemisorbed alkyl chains by thermal hydrosilylation of terminal alkenes.⁴⁰

Organic Ligand Passivation of the Si Nanocrystal Surface. The hydrogen-terminated Si nanocrystals obtained from the oxide etching step were passivated with an aliphatic ligand shell by use of a solution with a 4:1 ratio of 1-dodecene ($\text{C}_{12}\text{H}_{24}$) to 1-octadecene ($\text{C}_{18}\text{H}_{36}$). In most literature reports,

Si nanocrystals are passivated by use of alkenes with only a single chain length. The combination of long and short alkenes was found to enhance the ligand surface coverage and colloidal stability of Si nanocrystals greater than ~ 8 nm. Covalent attachment of the alkenes to the nanocrystal surface was achieved after heating at 190 $^{\circ}\text{C}$ for 8 h under nitrogen.¹³ After approximately 30 min at 190 $^{\circ}\text{C}$, the dispersions became clear, indicating successful attachment of the alkene to the surface. Nanocrystals produced by HSQ decomposition at 1350 $^{\circ}\text{C}$ formed stable dispersions in nonpolar organic solvent; however, the much larger (≥ 20 nm) nanocrystals produced at 1400 $^{\circ}\text{C}$ settled out of solution. The Si nanocrystal surface was characterized by X-ray photoelectron spectroscopy (XPS) prior to etching and after hydrosilylation. Figure 2 shows

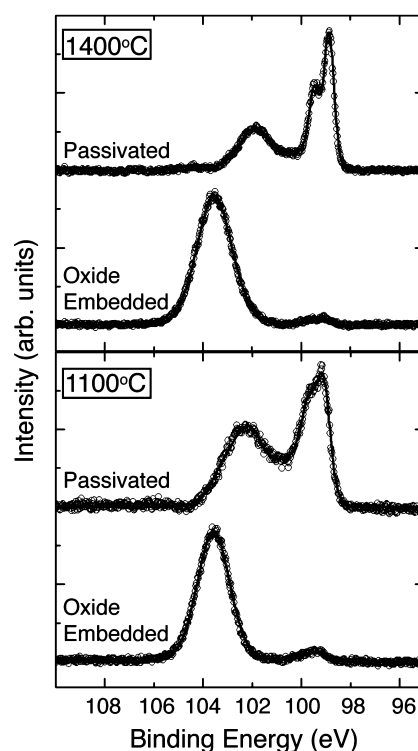


Figure 2. XPS of oxide-embedded and alkene-passivated Si nanocrystals synthesized at 1400 $^{\circ}\text{C}$ (top) and 1100 $^{\circ}\text{C}$ (bottom). A Shirley background subtraction was used for the data (O) and the best fit (solid line). The XPS spectra of oxide-embedded and alkene-passivated Si nanocrystals were taken 2 months after synthesis.

representative XPS spectra of Si nanocrystal samples prepared at 1100 and 1400 $^{\circ}\text{C}$. The as-prepared oxide-embedded nanocrystals exhibit prominent peaks characteristic of elemental Si and SiO_2 at ~ 99.5 and ~ 103.5 eV, respectively.^{3,29} After etching and hydrosilylation, two peaks are present in the XPS data at ~ 99.5 and ~ 102.0 eV, with a small shoulder at 103.5 eV. The peak at 102.0 eV is attributed to Si–C bonding at the nanocrystal surface, consistent with previous studies of alkyl-passivated Si nanocrystals and silicon carbide (Si–C) nanocrystals or thin films.^{13,41,42} The small shoulder at 103.5 eV, more pronounced in the spectrum of the 1100 $^{\circ}\text{C}$ sample, corresponds to suboxide species that form during the handling and clean-up procedures. This residual surface oxidation also appears in fourier transform infrared (FTIR) spectra of the nanocrystals (data not shown) as an Si–O–Si stretch, as we have reported previously.¹³

A rigorous purification procedure was necessary to obtain clear TEM images of the nanocrystals and ensure the samples were free of impurities prior to optical characterization. Alkyl-passivated Si nanocrystals have previously been purified with high-pressure filtration and column chromatography,^{11,18,36} and in some cases by dialysis or biphasic extraction.^{24,43} We found that precipitation with the solvent/antisolvent pairs of toluene/acetone or toluene/methanol was very effective in removing excess 1-dodecene and 1-octadecene and other impurities. The solvent/antisolvent washing procedure was repeated at least four times to obtain clean nanocrystal samples. The larger nanocrystals were more easily purified than smaller ones. To remove residual ligand, the nanocrystals were dried into a film on the inside of a round-bottom flask heated under vacuum for 24 h at 200 °C. The resulting nanocrystals dispersed readily in toluene.

Transmission Electron Microscopy of Si Nanocrystals on Graphene. Reliable TEM data for Si nanocrystals have been challenging to obtain, due in part to the low *z*-contrast of Si against the carbon used as a support for TEM samples. Excess ligand retained in nanocrystal samples also makes imaging difficult. In order to obtain Si lattice resolution, TEM imaging conditions are typically used that maximize resolution at the expense of higher contrast. By using a low accelerating voltage (≤ 120 kV), employing a rigorous cleaning procedure and sample preparation technique, and supporting the Si nanocrystals on graphene, TEM images of Si nanocrystals were obtained with high degree of clarity and enabled a clear determination of their size, crystallinity, and morphology.

Figure 1 shows TEM images of various alkene-passivated Si nanocrystals synthesized at a range of peak reaction temperatures. Images were collected on a FEI Tecnai Spirit Bio Twin TEM configured for biological samples operated at 80 kV. Table 1 summarizes the average diameter and polydispersity of

qualitative changes in the particle growth mechanism. These issues are still under investigation.

Figure 3 shows high-resolution bright-field and high-angle annular dark-field (HAADF) STEM images of alkene-passivated Si nanocrystals supported on graphene from an aberration-corrected STEM operated at 120 kV. HRTEM images acquired at 200 kV with standard carbon-coated TEM grids were considerably less clear and more difficult to obtain. HAADF STEM images in Figure 3B,C,G show enhanced contrast compared to bright-field images, more clearly differentiate between the nanocrystals and the graphene support, and allow for imaging extended fields of nanocrystals (90 000 nm²). Figure 3E–G show the image clarity is further enhanced by imaging nanocrystals over vacuum, where the ligand shell can be differentiated from nanocrystal surface. Lattice resolution was observed in both bright-field and HAADF imaging configurations.

X-ray Diffraction. Figure 4 shows XRD data for alkene-passivated Si nanocrystals produced at various HSQ decomposition temperatures. All of the XRD patterns index to diamond cubic Si, with significant size-dependent peak broadening. The broad reflection at 2θ of approximately 20° results from the surface alkyl ligands. The peak broadening can be used to determine the nanocrystal size by employing the Scherrer equation:⁴⁴

$$D = \frac{K\lambda}{B \cos \theta} \quad (1)$$

In eq 1, *D* is the nanocrystal diameter, *K* is a constant related to particle morphology and is typically 0.9 for spherical particles, *B* is the full width at half-maximum (fwhm) of the Bragg peak, and θ is the center position of the Bragg peak. Table 1 lists the average diameters of the Si nanocrystal samples determined by Scherrer analysis of the XRD peak broadening compared to the sizes determined by TEM and SAXS. There is little deviation in size between the various measurements, except for the nanocrystals produced at 1400 °C. The Scherrer analysis of the XRD data gave an average diameter of 18.2 nm, but TEM images (Figure 1 G) showed that there are clearly much larger nanocrystals present in the sample as well, with widely varying size from 18 to 90 nm.

Small-Angle X-ray Scattering. Small angle X-ray scattering (SAXS) can provide a statistically accurate determination of nanocrystal size distributions.^{13,45} Figure 5 shows the SAXS data of several alkene-passivated Si nanocrystal samples dispersed in toluene. Table 1 summarizes the average diameter and standard deviation (size distribution) obtained by fitting the SAXS data in Figure 5 with a spherical particle model using a Gaussian size distribution (eq 1).¹³ The scattering intensity *I*(*q*), from a dilute dispersion of scatterers, is

$$I(q) \propto \int_0^\infty N(R)P(qR)R^6 dR \quad (2)$$

where the form factor for solid homogeneous spheres is $P(qR) = \{3[\sin(qR) - qR \cos(qR)]/(qR)^3\}^2$. The scattering wave vector *q*, depends on the X-ray wavelength λ and scattering angle θ : $q = (4\pi/\lambda) \sin(\theta/2)$.^{46–49} *N*(*R*) is the number fraction of nanocrystals of radius *R*, in the sample, assumed to have a Gaussian distribution: $N(R) = \{1/[\sigma(2\pi)^{1/2}]\} \exp[-(R - \bar{R})^2/(2\sigma^2)]$. \bar{R} is the average nanocrystal radius and σ is the standard deviation of the size distribution.

The average diameters determined from SAXS are similar to those determined by Scherrer analysis of XRD peak broadening

Table 1. Summary of Si Nanocrystal Size^a

reaction temp (°C)	particle diameter (nm)		
	TEM	XRD	SAXS
1100	3.1 ± 0.3	2.7	2.7 ± 0.6
1150	4.2 ± 0.6	3.3	2.9 ± 1.0
1200	7.3 ± 1.0	5.1	5.0 ± 1.3
1250	7.0 ± 1.0	5.5	6.0 ± 1.7
1300	10.3 ± 1.3	7.9	8.8 ± 1.8
1350	12.8 ± 2.4	10.2	11.8 ± 2.1
1400	<i>b</i>	18.2	

^aDetermined from SAXS, TEM, and Scherrer analysis of XRD peak broadening. ^bPolydisperse.

the nanocrystals as determined from TEM. The nanocrystal size increased steadily with higher peak reaction temperature. Nanocrystals synthesized at temperatures of 1350 °C and lower were relatively monodisperse with standard deviations about the mean diameter ranging between 10% and 19%, without any postsynthesis size selection. Nanocrystals obtained from the higher temperature reactions at 1400 °C were very polydisperse and significantly larger, with particle diameters ranging from 18 to 90 nm (Figure 1G). These larger nanocrystals also exhibited noticeable faceting. The reactions carried out close to the melting temperature of Si (1414 °C) exhibit a rather dramatic increase in nanocrystal size, which is perhaps from a significant softening of the SiO₂ matrix, which could also lead to

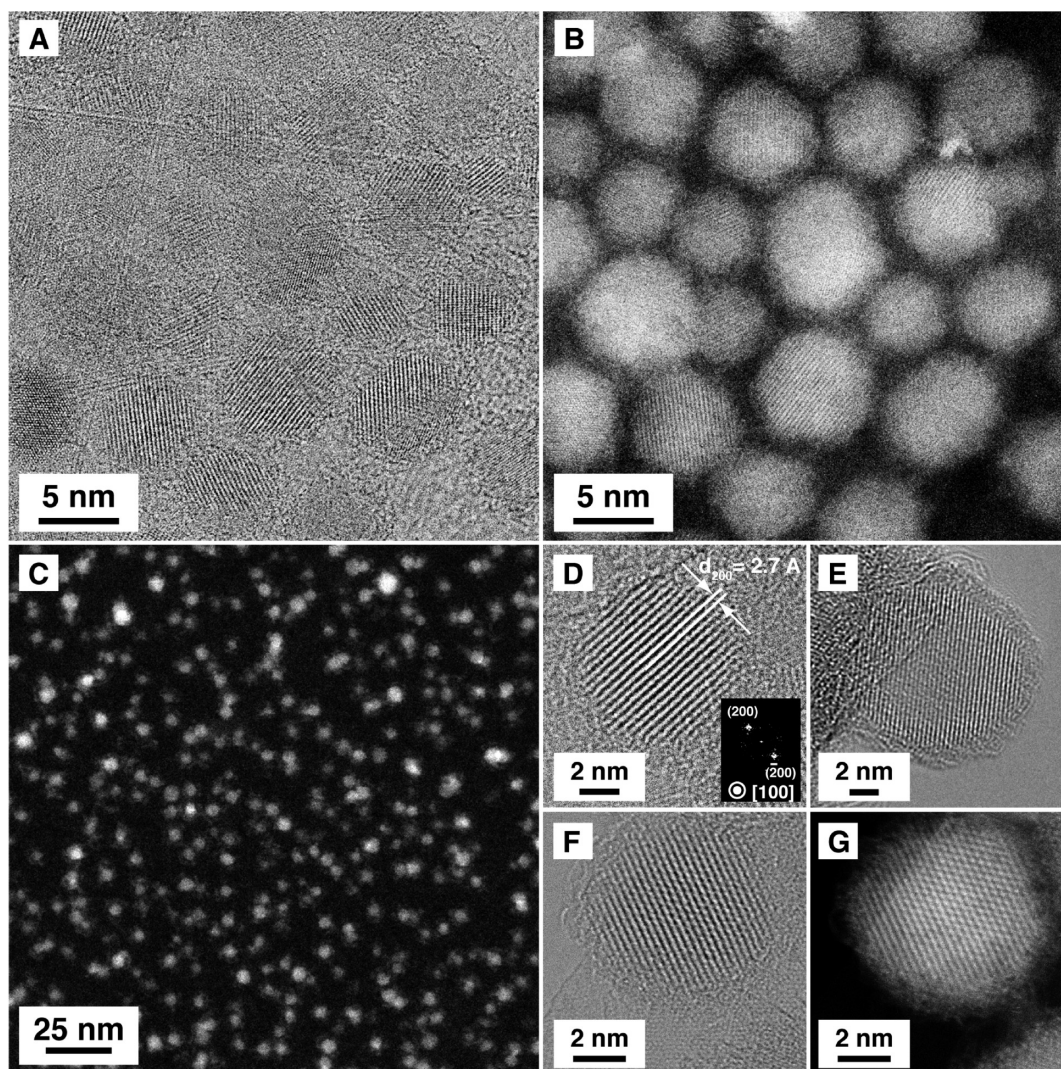


Figure 3. (A, D–F) High-resolution bright-field and (B, C, G) HAADF STEM images of alkene-passivated Si nanocrystals. Image C shows Si nanocrystals synthesized at 1100 °C, while the remaining images are of samples produced at 1250 °C. The fast Fourier transform (FFT) in the inset of panel D) indexes to diamond structure Si, with measured d -spacings of 2.7 Å that correspond to (200) lattice planes with a [100] zone axis.

but are slightly smaller than those determined from TEM images. The size polydispersity is also slightly larger, ranging from 18% to 33%. In the case of the larger nanocrystals, there was more deviation between the model fits and the SAXS data at higher q .

Optical Properties. *UV–vis–NIR Absorbance Spectroscopy.* Room-temperature UV–vis–NIR absorbance spectra were measured for Si nanocrystals dispersed in toluene at various concentrations to determine the molar extinction coefficients (ϵ) of the nanocrystals shown in Figure 6. The absorbance spectra are essentially featureless. In this size range, the nanocrystals still behave essentially as indirect band-gap semiconductors.^{50,51} The absorption cross-section increases by orders of magnitude with relatively small changes in wavelength. For example, the molar extinction coefficients at 400 nm near PLE maxima range from $3 \times 10^4 \text{ M}^{-1}\cdot\text{cm}^{-1}$ for the 3 nm diameter nanocrystals to greater than $1 \times 10^6 \text{ M}^{-1}\cdot\text{cm}^{-1}$ for the 12 nm diameter nanocrystals. At NIR wavelengths, the region where human tissue is relatively transparent, the absorption is a few orders of magnitude lower but is still significant: at 650 nm, $\epsilon = 4 \times 10^2 \text{ M}^{-1}\cdot\text{cm}^{-1}$ for the smallest nanocrystals and increases up to values of $\epsilon = 2 \times 10^5 \text{ M}^{-1}\cdot\text{cm}^{-1}$ for the largest

nanocrystals, which are comparable to the molar absorption coefficients of direct band-gap semiconductor nanocrystals like CdX (X = S, Se, Te) with molar absorption coefficients between 2 and $5 \times 10^5 \text{ M}^{-1}\cdot\text{cm}^{-1}$ at the excitonic maxima.⁵²

Photoluminescence Spectroscopy. Figure 7 shows room-temperature PL and PLE spectra of octadecene/dodecene-stabilized Si nanocrystals. As summarized in Table 2, the PL emission peaks range from approximately 720 nm (3 nm diameter) out to 1060 nm (12 nm diameter), near the bulk band gap of Si, with quantum yields of 8% for the smallest (3 nm diameter) nanocrystals decreasing with increasing diameter down to 0.4% for the 12 nm nanocrystals. A decrease in PL QY with increasing size has also been observed from other types of nanocrystals as well. For the largest light-emitting nanocrystals, the line shape of the PL peak becomes non-Gaussian with a noticeable drop in intensity at ~ 1150 nm, which may be the fundamental long-wavelength limit for emission from alkyl-passivated Si nanocrystals. Nanocrystals larger than about 12 nm did not have measurable PL. Note also that the QY of the Si nanocrystal PL is relatively high compared to organic fluorophores, as few molecular dyes exist that emit in this wavelength range.^{34,53} This is important with respect to

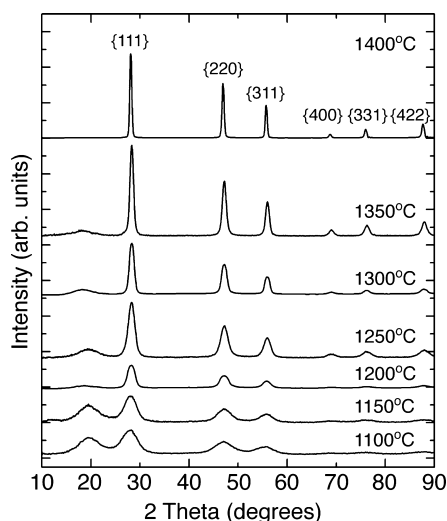


Figure 4. XRD of alkene-passivated Si nanocrystals that were synthesized by HSQ decomposition at the noted temperatures. The diffraction patterns correspond to diamond cubic Si (JCPDS no. 027-1402; $a = b = c = 5.43$ Å).

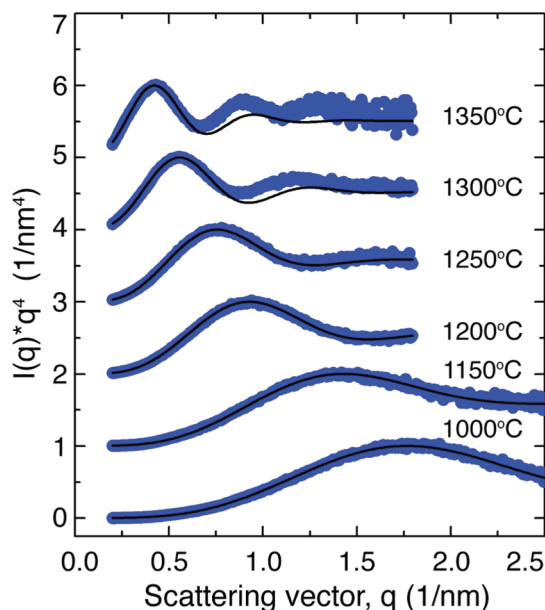


Figure 5. SAXS data (blue circles), shown as Porod plots of $I(q) \times q^4$ vs q , for alkene-passivated Si nanocrystals dispersed in toluene. The scattering intensity is normalized to the intensity of the first peak maximum, and traces are offset vertically for clarity. Black lines are the best-fit curves by use of eq 1 to each data set to determine the size parameters in Table 1.

biological imaging applications, in which biocompatible contrast agents with NIR emission are desirable.

Relationship between PL Peak Energy and Si Nanocrystal Size. Unlike the case of nanocrystals of direct band-gap semiconductors like CdSe and InAs, it is difficult to determine the absorption onset of Si nanocrystals. Because Si has an indirect band gap, sharp exciton peaks do not appear in the absorbance spectra.⁵⁴ The amount of light absorption near the optical gap in Si nanocrystals is also very low and difficult to detect, even in very concentrated nanocrystal dispersions. This results in a very large *apparent* Stokes shift between the PLE and PL, as in Figure 7 (more than 500 nm for the 12 nm

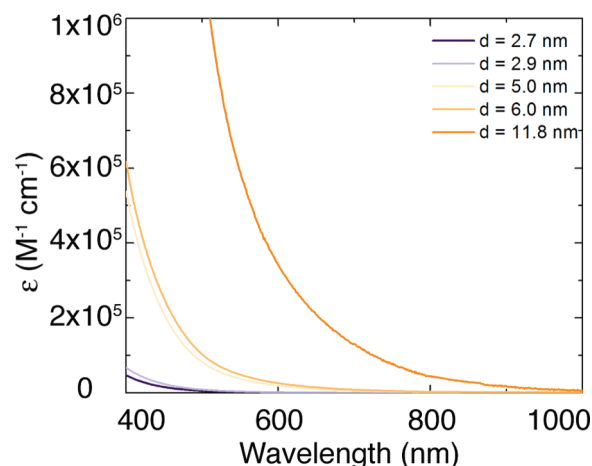


Figure 6. Molar absorption coefficients (ϵ) of Si nanocrystals with the indicated diameters. Raw absorbance data and calculations for determining the molar absorption coefficients are included in the Supporting Information.

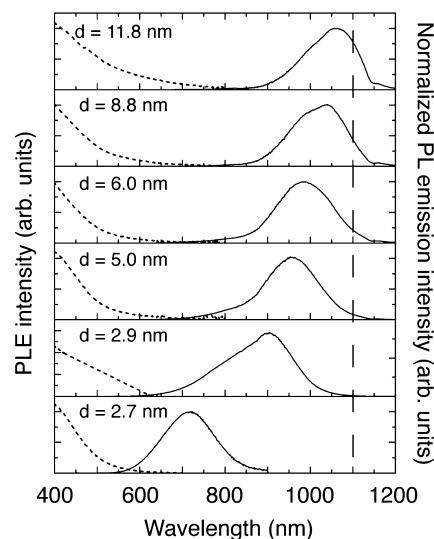


Figure 7. Room-temperature PL ($\lambda_{\text{exc}} = 420$ nm) and PLE (measured at emission maximum) spectroscopy of alkane-stabilized Si nanocrystals dispersed in toluene. The nanocrystal diameter determined by SAXS is indicated near each curve. The spectra have been normalized in intensity to demonstrate the peak shift with processing temperature. For PLE spectra, a reference silicon photodiode was used to adjust for intensity differences in the lamp spectrum for the measurements. The vertical dashed line indicates the position of the bulk Si band gap (1100 nm).

diameter nanocrystals!). As explained by Kovalev, this *apparent* Stokes shift between the absorption (or PLE) onset and the PL peak is actually an artifact of the very low density of states near the band edge. For Si nanocrystals in this size range, the absorption cross-section changes by a few orders of magnitude from the band edge with relatively small changes in wavelength. As one would expect, quantum confinement does lead to a noticeable blue shift in the absorption—this is seen, for example, by comparing the size-dependent PLE data in Figure 7—but the light absorption dies off rapidly with wavelength and it becomes very difficult to obtain an accurate measure of the absorption edge. Therefore, as Kovalev et al.⁵¹ suggest, we use the PL peak energy as a measure of the exciton energy of the nanocrystals and plot this in Figure 8 as a function of size

Table 2. Summary of PL Spectroscopic Data for Si Nanocrystals^a

reaction temp (°C)	particle diameter (nm) by SAXS	PL max (nm) for $\lambda_{\text{ex}} = 420$ nm	quantum yield (%) via IR-26
1100	2.7 ± 0.6	718	8
1150	2.9 ± 1.0	903	5
1200	5.0 ± 1.3	957	3
1250	6.0 ± 1.7	986	1
1300	8.8 ± 1.8	1035	0.6
1350	11.8 ± 2.1	1064	0.4

^aNanocrystals were synthesized at various reaction temperatures having the indicated diameters determined by SAXS. The quantum yield was determined by direct comparison with IR-26, a NIR-emitting dye.

determined by SAXS. Figure 8 also shows the size-dependent PL peak energy calculated with the effective mass approx-

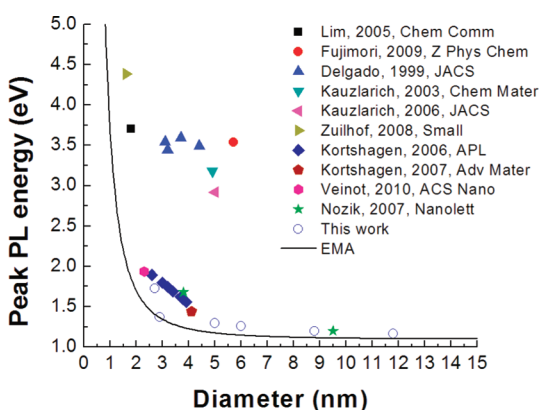


Figure 8. PL peak emission versus Si nanocrystal diameter for our work (○) and a number of literature reports (solid symbols) of alkyl-passivated Si nanocrystals. The curve corresponds to the effective mass approximation (EMA). In our samples, PL could not be detected from nanocrystals much larger than 12 nm in diameter.

imation (EMA):^{55,56}

$$E(d) = E_g + \frac{\hbar^2 \pi^2}{2d^2} \left(\frac{1}{m_e^*} + \frac{1}{m_h^*} \right) - \frac{1.786e^2}{\epsilon_r d} \quad (3)$$

In eq 3, d is the nanocrystal diameter, e is the electron charge, ϵ_r is the relative permittivity of Si (11.68), and m_e^* and m_h^* are the effective masses of the electron and hole, equal to $0.19m_0$ and $0.286m_0$, respectively. The EMA is most easily solved by converting to atomic units of measure, where $\hbar = e = m_0 = 1$, and length is given in terms of the Bohr radius (1 au = 0.0529 nm). The EMA calculations provide a reasonable estimate of the observed size-dependent PL of the Si nanocrystals made in this study over a relatively wide range of sizes.

For comparison, Figure 8 also shows the PL peak energy of Si nanocrystals reported from a number of other studies of alkyl-passivated Si nanocrystals. A number of data points from the literature occur at noticeably higher energy. These data, exhibiting blue-light emission and a noticeable lack of size dependence in emission wavelength, all correspond to nanocrystals produced by a low-temperature solution-phase arrested precipitation by chemical reduction of SiCl_4 ^{20,24,57} or oxidation of Zintl salts.^{21–23} Presently, it is not known why these particular nanocrystals emit only blue or UV light and

exhibit limited wavelength tunability,⁵⁸ while Si nanocrystals produced by synthetic routes employing higher reaction and growth temperatures have tended to emit light at much redder wavelengths at comparable sizes. One issue is that the PL of Si nanocrystals is well-known to be very sensitive to the surface chemistry, particularly the presence of oxide.³² However, Delerue and co-workers³¹ have shown that trap states from Si–O species on the nanocrystal surface reside above the bottom of the conduction band and below the top of the valence band and should not significantly affect the PL from nanocrystals greater than 3 nm in diameter.

CONCLUSIONS

We have demonstrated that it is possible to produce fairly monodisperse colloidal Si nanocrystals with diameters tailored from 3 to 90 nm that emit in the red and NIR spectral region. The HSQ method reported here yields a wide range of PL, with tunable PL emission from about 530 nm^{3,29} up to 1060 nm. Accurate measurements of the nanocrystal size were obtained by TEM imaging on graphene supports combined with complementary SAXS and XRD measurements. The rigorous cleaning procedure we describe was essential for obtaining reliable TEM data and PL data from samples that were free of impurities. The measured PL energy was then correlated with size and compared to the data reported in the literature and the EMA. There is good agreement between the size-correlated emission data from other high-temperature syntheses in the literature and the EMA calculations. We show the upper size threshold for efficient light emission from alkyl-passivated Si nanocrystals is approximately 12 nm in diameter.

The optical data reported here are relevant to studies using luminescent Si nanocrystals as contrast agents for the detection of disease. Si nanomaterials have received notable attention for their applicability in medicine because they are biocompatible and biodegradable, which is a significant advantage over heavy metal-containing quantum dots such as CdSe.⁵⁹ Si nanocrystals exhibit size-tunable emission with red to NIR wavelength, but there is a large wavelength difference between the emitting wavelengths and the wavelengths needed for excitation with strong emission. This presents a major challenge. For example, the region of strong light absorption for high brightness emission in the case of small (2–3 nm) Si nanocrystals occurs below about 500 nm, which overlaps with the absorption of water, hemoglobin, and oxyhemoglobin in human tissue.⁶⁰ This limits the applicability of small Si nanocrystals for single-photon bioimaging applications. Our data show that this limitation can be overcome by shifting the absorption to the red with increased Si nanocrystal size. The PL quantum yield decreases slightly as the nanocrystal size increases; however, it remains relatively high compared to other NIR emitters.^{34,53}

ASSOCIATED CONTENT

Supporting Information

Additional text, two figures, and one table with detailed descriptions of how the molar extinction coefficients and photoluminescence quantum yields were calculated. This material is available free of charge via the Internet at <http://pubs.acs.org>.

AUTHOR INFORMATION

Corresponding Author

*Telephone +1-512-471-5633; fax +1-512-471-7060; e-mail korgel@che.utexas.edu.

ACKNOWLEDGMENTS

We acknowledge financial support of this work from the National Science Foundation (Grant 0618242), the National Science Foundation NNIN Program (Grant ECCS-0335765), the Robert A. Welch Foundation (Grant F-1464), and the Natural Science and Engineering Research Council of Canada. H.F. also acknowledges support through the Nanotechnology Network Program of MEXT under Project 3 NIM-08F-001. We thank G. Casillas for assistance with STEM imaging, Eric Henderson for discussions pertaining to Si nanocrystal etching, and Andy Heitsch for insightful discussions.

REFERENCES

- (1) Canham, L. T. *Appl. Phys. Lett.* **1990**, *57*, 1046–1048.
- (2) Cullis, A. G.; Canham, L. T.; Calcott, P. D. *J. Appl. Phys.* **1997**, *82*, 909–965.
- (3) Hessel, C. M.; Henderson, E. J.; Veinot, J. G. C. *Chem. Mater.* **2006**, *18*, 6139–6146.
- (4) Li, X.; He, Y.; Talukdar, S. S.; Swihart, M. T. *Langmuir* **2003**, *19*, 8490–8496.
- (5) Pi, X. D.; Liptak, R. W.; Deneen Nowak, J.; Wells, N. P.; Carter, C. B.; Campbell, S. A.; Kortshagen, U. *Nanotechnology* **2008**, *19*, No. 245603.
- (6) Sykora, M.; Mangolini, L.; Schaller, R. D.; Kortshagen, U.; Jurbergs, D.; Klimov, V. I. *Phys. Rev. Lett.* **2008**, *100*, 067401.
- (7) Puzzo, D. P.; Henderson, E. J.; Helander, M. G.; Wang, Z. B.; Ozin, G. A.; Lu, Z. H. *Nano Lett.* **2011**, *11*, 1585–1590.
- (8) Cheng, K. Y.; Anthony, R.; Kortshagen, U. R.; Holmes, R. J. *Nano Lett.* **2011**, *11*, 1952–1956.
- (9) Cheng, K. Y.; Anthony, R.; Kortshagen, U. R.; Holmes, R. J. *Nano Lett.* **2010**, *10*, 1154–1157.
- (10) Canham, L. T. *Adv. Mater.* **1995**, *7*, 1033–1037.
- (11) Erogbogbo, F.; Yong, K. T.; Roy, L.; Xu, G. X.; Prasad, P. N.; Swihart, M. T. *ACS Nano* **2008**, *2*, 873–878.
- (12) Park, J. H.; Gu, L.; Von Maltzahn, G.; Ruoslahti, E.; Bhatia, S. N.; Sailor, M. J. *Nat. Mater.* **2009**, *8*, 331–336.
- (13) Hessel, C. M.; Rasch, M. R.; Hueso, J. L.; Goodfellow, B. W.; Akhavan, V. A.; Puvanakrishnan, P.; Tunnel, J. W.; Korgel, B. A. *Small* **2010**, *6*, 2026–2034.
- (14) Heath, J. R. *Science* **1992**, *258*, 1131–1133.
- (15) English, D. S.; Pell, L. E.; Yu, Z. H.; Barbara, P. F.; Korgel, B. A. *Nano Lett.* **2002**, *2*, 681–685.
- (16) Holmes, J. D.; Ziegler, K. J.; Doty, R. C.; Pell, L. E.; Johnston, K. P.; Korgel, B. A. *J. Am. Chem. Soc.* **2001**, *123*, 3743–3748.
- (17) Pell, L.; Korgel, B. *Proc. SPIE* **2002**, *4808*, 91–98.
- (18) Littau, K. A.; Szajowski, P. J.; Muller, A. J.; Kortan, A. R.; Brus, L. E. *J. Phys. Chem.* **1993**, *97*, 1224–1230.
- (19) Tilley, R. D.; Warner, J. H.; Yamamoto, K.; Matsui, I.; Fujimori, H. *Chem. Commun.* **2005**, 1833–1835.
- (20) Teh, G. B.; Saravanan, N.; Tilley, R. D.; Ramesh, S.; Lim, Y. S. *Z. Phys. Chem. (Muenchen)* **2009**, *223*, 1417–1426.
- (21) Yang, C. S.; Bley, R. A.; Kauzlarich, S. M.; Lee, H. W. H.; Delgado, G. R. *J. Am. Chem. Soc.* **1999**, *121*, 5191–5195.
- (22) Pettigrew, K. A.; Liu, Q.; Power, P. P.; Kauzlarich, S. M. *Chem. Mater.* **2003**, *15*, 4005–4011.
- (23) Neiner, D.; Chiu, H. W.; Kauzlarich, S. M. *J. Am. Chem. Soc.* **2006**, *128*, 11016–11017.
- (24) Rosso-Vasic, M.; Spruijt, E.; Van Lagen, B.; De Cola, L.; Zuilhof, H. *Small* **2008**, *4*, 1835–1841.
- (25) Jurbergs, D.; Rogojina, E.; Mangolini, L.; Kortshagen, U. *Appl. Phys. Lett.* **2006**, *88*, No. 233116.
- (26) Li, X. G.; He, Y. Q.; Talukdar, S. S.; Swihart, M. T. *Langmuir* **2003**, *19*, 8490–8496.
- (27) Gupta, A.; Swihart, M.; Wiggers, H. *Adv. Funct. Mater.* **2009**, *19*, 696–703.
- (28) Mangolini, L.; Thimsen, E.; Kortshagen, U. *Nano Lett.* **2005**, *5*, 655–659.
- (29) Hessel, C. M.; Henderson, E. J.; Veinot, J. G. C. *J. Phys. Chem. C* **2007**, *111*, 6956–6961.
- (30) Henderson, E. J.; Kelly, J. A.; Veinot, J. G. C. *Chem. Mater.* **2009**, *21*, 5426–5434.
- (31) Wolkin, M. V.; Jorne, J.; Fauchet, P. M.; Allan, G.; Delerue, C. *Phys. Rev. Lett.* **1999**, *82*, 197–200.
- (32) Gupta, A.; Swihart, M. T.; Wiggers, H. *Adv. Funct. Mater.* **2009**, *19*, 696–703.
- (33) Hessel, C. M.; Henderson, E. J.; Kelly, J. A.; Cavell, R. G.; Sham, T. K.; Veinot, J. G. C. *J. Phys. Chem. C* **2008**, *112*, 14247–14254.
- (34) Semonin, O. E.; Johnson, J. C.; Luther, J. M.; Midgett, A. G.; Nozik, A. J.; Beard, M. C. *J. Phys. Chem. Lett.* **2010**, *1*, 2445–2450.
- (35) Kelly, J. A.; Veinot, J. G. C. *ACS Nano* **2010**, *4*, 4645–4656.
- (36) Hua, F.; Swihart, M. T.; Ruckenstein, E. *Langmuir* **2005**, *21*, 6054–6062.
- (37) Kolasinski, K. W. *Surf. Sci.* **2009**, *603*, 1904–1911.
- (38) Doan, V. V.; Penner, R. M.; Sailor, M. J. *J. Phys. Chem.* **1993**, *97*, 4505–4508.
- (39) Heinrich, J. L.; Curtis, C. L.; Credo, G. M.; Kavanagh, K. L.; Sailor, M. J. *Science* **1992**, *255*, 66–68.
- (40) Buriak, J. M. *Chem. Rev.* **2002**, *102*, 1271–1308.
- (41) Henderson, E. J.; Veinot, J. G. C. *J. Am. Chem. Soc.* **2009**, *131*, 809–815.
- (42) Avila, A.; Montero, I.; Galan, L.; Ripalda, J. M.; Levy, R. *J. Appl. Phys.* **2001**, *89*, 212–216.
- (43) Zhang, X.; Neiner, D.; Wang, S.; Louie, A. Y.; Kauzlarich, S. M. *Nanotechnology* **2007**, *18*, No. 095601.
- (44) Zsigmondy, R.; Scherrer, P. *Kolloidchemie*, 3rd ed.; Spamer: Leipzig, Germany, 1920.
- (45) Kelly, J. A.; Shukaliak, A. M.; Fleischauer, M. D.; Veinot, J. G. C. *J. Am. Chem. Soc.* **2011**, *133*, 9564–9571.
- (46) Korgel, B. A.; Fitzmaurice, D. *Phys. Rev. B* **1999**, *59*, 14191–14201.
- (47) Korgel, B. A.; Fullam, S.; Connolly, S.; Fitzmaurice, D. *J. Phys. Chem. B* **1998**, *102*, 8379–8388.
- (48) Glatter, O.; Kratky, O., Eds. *Small-Angle X-ray Scattering*. Academic Press: New York, 1982.
- (49) Guinier, A.; Fournet, G. *Small-angle Scattering of X-rays*; Wiley: New York, 1955.
- (50) Beard, M. C.; Knutsen, K. P.; Yu, P. R.; Luther, J. M.; Song, Q.; Metzger, W. K.; Ellingson, R. J.; Nozik, A. J. *Nano Lett.* **2007**, *7*, 2506–2512.
- (51) Kovalev, D.; Diener, J.; Heckler, H.; Polisski, G.; Kunzner, N.; Koch, F. *Phys. Rev. B* **2000**, *61*, 4485–4487.
- (52) Yu, W. W.; Qu, L. H.; Guo, W. Z.; Peng, X. G. *Chem. Mater.* **2003**, *15*, 2854–2860.
- (53) Steckel, J. S.; Coe-Sullivan, S.; Bulovic, V.; Bawendi, M. G. *Adv. Mater.* **2003**, *15*, 1862–1866.
- (54) Wilson, W. L.; Szajowski, P. F.; Brus, L. E. *Science* **1993**, *262*, 1242–1244.
- (55) Efros, A. L. *Soviet Physics Semiconductors USSR* **1982**, *16*, 772–775.
- (56) Trwoga, P. F.; Kenyon, A. J.; Pitt, C. W. *J. Appl. Phys.* **1998**, *83*, 3789–3794.
- (57) Tilley, R. D.; Yamamoto, K.; Matsui, I.; Fujimori, H. *Chem. Commun.* **2005**, 1833–1835.
- (58) Shirahata, N.; Hasegawa, T.; Sakka, Y.; Tsuruoka, T. *Small* **2010**, *6*, 915–921.
- (59) Derfus, A. M.; Chan, W. C. W.; Bhatia, S. N. *Nano Lett.* **2004**, *4*, 11–18.
- (60) Weissleder, R. *Nat. Biotechnol.* **2001**, *19*, 316–317.